ELSEVIER

Contents lists available at ScienceDirect

Materials Science & Engineering A

journal homepage: www.elsevier.com/locate/msea





An experimental study of anisotropic fracture behavior of rolled AZ31B magnesium alloy under monotonic tension

Yuqian Wang, Qin Yu**, Yanyao Jiang

University of Nevada, Department of Mechanical Engineering, Reno, NV, 89557, USA

ARTICLE INFO

Keywords:
Magnesium alloy
Anisotropy
Fracture
Double twins
Twin-twin interaction

ABSTRACT

Wrought magnesium (Mg) alloys display pronounced anisotropy in their room-temperature mechanical responses. The fracture behavior of Mg alloys, especially its reliance of material orientation, has not been well explored. The current work is an investigation of the anisotropic fracture behavior in a rolled AZ31B Mg alloy by carrying out monotonic tension experiments of specimens taken from the rolled Mg plate with five different material orientations ($\theta=0^{\circ}$, 22.5°, 45°, 67.5° and 90°) with respect to the rolled direction (RD). Significant anisotropy is exhibited in the tensile fracture of the rolled Mg alloy. At the macroscopic scale, shear fracture displaying relatively flat fracture surface is exhibited from tension at $\theta=22.5^{\circ}$ and 45°. Microstructural analysis reveals that fracture at these two material orientations is a result of localized shearing accommodated by basal slips from which both crack initiation and propagation are originated. In contrast, under tension at $\theta=0^{\circ}$, 67.5° and 90°, brittle-like fracture is shown where irregular-shaped surfaces composed by ridges and islands are observed. For $\theta=0^{\circ}$, microstructural analysis in the vicinity of microcracks confirms that crack forms at the tip and/or boundary of compression and compression-tension double twins. For the cases of $\theta=67.5^{\circ}$ and 90°, microcrack initiation is due to high-angle grain boundary cracking, which is likely caused by stress concentration due to impingements of none co-zone twin-twin boundaries and tertiary tension-compression-tension twins on the high-angle grain boundaries.

1. Introduction

Magnesium (Mg) alloys are potential lightweight structural materials in automobile and aerospace industries to improve energy efficiency [1–7]. However, their application for load-bearing components is limited by the poor ductility and formability at ambient temperature due to the limited number of slip/twin systems in the hexagonal close packed (hcp) crystal structure of the materials. Plastic deformation resolved along the a-axis can be accommodated by basal $\langle a \rangle$, prismatic $\langle a \rangle$, and 1st order pyramidal $\langle a \rangle$ slips, whereas only $\{10\overline{1}2\}$ tension twin (or $\{10\overline{1}1\}$ compression twin) and 2nd order pyramidal $\langle a+c \rangle$ slips can accommodate plastic deformation along the c-axis. For wrought Mg alloys, a strong basal texture is often resulted from the rolling and extrusion processes. The basal texture, coupled with the pronounced variation in the critical resolved shear stresses (CRSSs) for different deformation modes, leads to significant mechanical anisotropy of Mg alloys. The anisotropic mechanical properties of Mg alloys have been

extensively documented with a concentration on the monotonic responses [8–21] and fatigue properties [22–41].

Few studies have been conducted on the fracture of Mg alloys under different loading directions with respect to the material texture [42–51]. Most of the prior work focused on studying the fracture behavior under monotonic or cyclic loading with the specimen oriented either along the rolled direction (RD), the extruded direction (ED), or the transverse direction (TD). Various fracture failures were reported depending on the specific material system and the loading direction. For instance, brittle fracture features with fine microscopic voids distributed on the fracture surface were reported in an AZ31B Mg alloy with tension along the RD [51] and in a Mg-5.72Al-2.96Zn-6.05Nd Mg alloy under tension along the ED [43]. However, for a pure Mg under tensile loading, the final fracture tends to show a shearing feature [47]. Similarly, typical shear fracture with different shearing angles was observed under in-plane compression applied to the AZ31B Mg specimens processed with various routes such as rolling, extrusion, and equal channel angular pressing (ECAP) [50].

 $^{^{\}ast}$ Corresponding author.

^{**} Corresponding author. Materials Sciences Division, Lawrence Berkeley National Laboratory, Berkeley, CA, 94720, USA. *E-mail addresses*: qin.yu.unr@gmail.com (Q. Yu), yjiang@unr.edu (Y. Jiang).

Pertaining to the fracture mechanisms, $\{10\overline{1}1\}-\{10\overline{1}2\}$ compressiontension (C-T) double twinning was regularly recognized as the potential sites of failure initiation [50-52] due to the large shear localization within the double twins, which is evidenced by the observation of obvious surface steps [51]. The lack of stress relaxation for the large local shear in the C-T double twinning causes micro-crack formation, usually leading to brittle fracture features [53]. However, certain shear fracture features formed in fine grains were also found to be originated from double twinning [54]. Other than C-T double twinning, fracture in Mg alloys is affected by other microstructural features. For example, the deformation incompatibilities caused by basal slip/tension twin blocked at twin and grain boundaries were considered to nucleate microvoids [47]. In addition, second-phase particle was reported to play a detrimental role on the final fracture [46]. As a grain-scale factor, grain refinement can lead to reduced twinning activity and may result in a lower microvoid growth rate [48].

Different observations of fracture mechanisms were made in wrought Mg alloys subjected to monotonic loading. A lack of consistency is likely caused by the microstructural diversity of different Mg alloys as well as the dissimilarity of the loading direction with respect to the texture. To seek a comprehensive understanding of the anisotropic fracture behavior of Mg alloy, we carried out monotonic tension experiments on a rolled AZ31B Mg alloy with specimens oriented in five material orientations with respect to the RD. Examinations into the micro-mechanisms associated with the anisotropic fracture behavior are discussed.

2. Experimental

2.1. Material and specimen

The material used in the current work is a commercially acquired hot-rolled plate of AZ31B Mg alloy with a thickness of 76.2 mm. The rolled direction, normal direction, and transverse direction are referred to as RD, ND, and TD, respectively. The three-dimensional (3-D) stereography of the as-rolled microstructure as shown in Fig. 1a is reconstructed from electron backscatter diffraction (EBSD) scans on three

orthotropic planes perpendicular to RD, ND, and TD, respectively. The average grain size is approximately 50 μm . The material displays an intense basal texture with the $c\text{-}\mathrm{axes}$ of most grains aligning parallel to the ND (Fig. 1b). No tension twins are present in the initial microstructure.

Solid cylindrical dog-bone shaped specimens were machined from the rolled plate with their loading axes (Z-axes) aligning, respectively, to the directions with $\theta=0^\circ$ (RD), $22.5^\circ, 45^\circ, 67.5^\circ$ and 90° (ND) with respect to the RD (Fig. 1c) on the ND-RD plane. To facilitate discussion, the coordinate system XYZ is embedded with the testing specimen following the convention that the YZ plane is parallel to the ND-RD plane and the Z axis is along the axial direction of the specimen. The X-axis is along the TD. The dog-bone shaped specimen used for tension experiment has a gage section length of 14 mm and a cross-sectional diameter of 8.0 mm. Before mechanical testing, the surface of the gage section was polished by using silicon carbide papers with grit No. from P400 up to P1200.

2.2. Mechanical experiments

Monotonic tension experiments were carried out in ambient air using a servo-hydraulic load frame. The engineering strain was measured by a clip-on extensometer attached to the specimen surface within the gage section. Monotonic tension was applied by the displacement control corresponding to an approximate strain rate of $8\times 10^{-4} s^{-1}$. For each loading case, two specimens were tested to ensure the reliability of the stress-strain responses as well as the similarity of the featured fracture behavior.

2.3. Material characterization

After a specimen was broken into two parts, the macroscopic profile of the fracture surface was reconstructed by stacking multiple optical images captured at different focus heights using a Keyence 3-D digital microscope VHX-5000. To discern the crack initiation and early-stage growth mechanisms, microstructure in the vicinity of the microcracks was characterized in the region near the macroscopic fracture surface

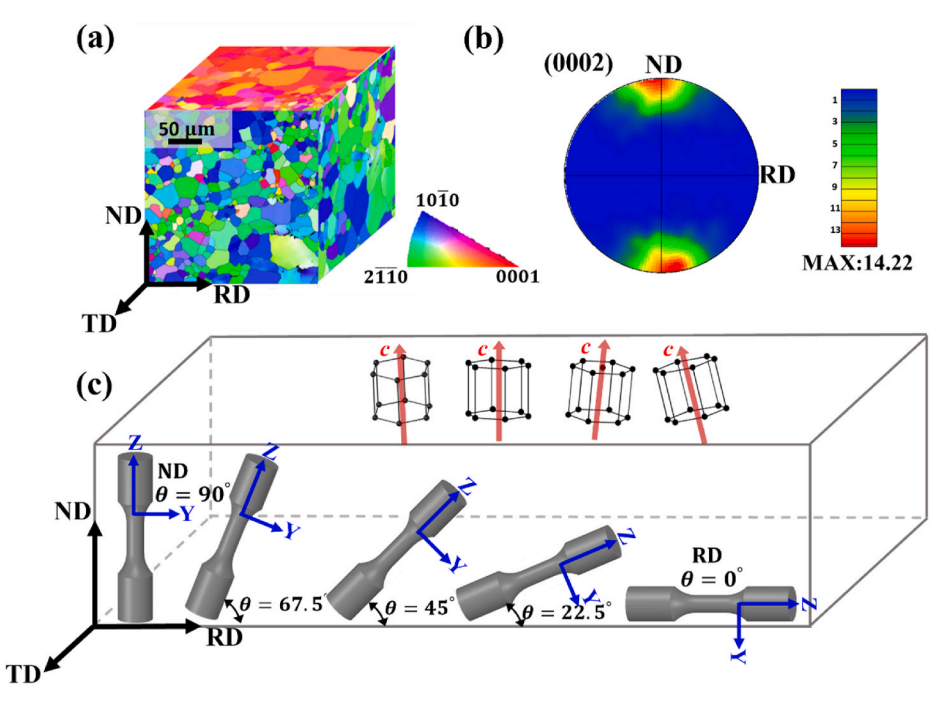


Fig. 1. Microstructure of the rolled AZ31B Mg alloy and testing specimens. (a) Three-dimensional stereograph of the as-rolled microstructure; (b) {0001} pole figure; (c) Cylindrical dog-bone shaped specimen with loading axes aligned at five different orientations with $\theta = 0^{\circ}$ (RD), 22.5°, 45°, 67.5° and 90° (ND) relative to the rolled direction.

using a field emission scanning electron microscope (SEM) and EBSD scanning. The samples for EBSD analysis were cut along the diametral direction within the region approximately 500 µm away from the fracture surface. The scan plane of the EBSD sample is parallel to the YZ plane, which is perpendicular to the TD (Fig. 1c). The samples were mechanically ground using silicon carbide papers with grit No. from P500 to P1500, followed by polishing using diamond suspension with particle sizes of 6 µm and 1 µm. After a final polishing using alumina with particle size of $0.05~\mu m$, the sample surface was etched with 3%Nital for 8s. The EBSD scans were taken by Joel 7100 F SEM equipped with an Oxford HKL Channel 5 EBSD detector at an acceleration voltage of 25 kV. The working distance was 24 mm. The step size for large scans of 250 \times 250 μm^2 was 0.5 μm . Two large scans with an area of 250 $\mu m \times$ 250 µm were obtained to derive the average twin volume fraction (TVF) for each loading condition. A smaller step size of 0.25 µm was used for high resolution scans specifically to capture the microstructure feature surrounding microcracks.

3. Results and discussion

3.1. Deformation features under tension

The engineering stress-strain responses of the specimens obtained under monotonic tension in five different orientations are shown in Fig. 2. The {0001} pole figures along with the tension twin volume fractions (TVFs) corresponding to different testing specimens after tensile fracture are indicated in Fig. 2.

As shown in Fig. 2a, tensile stress-strain curves for $\theta < 45^\circ$ exhibit an overall concave-down shape. The plastic deformation is accommodated mostly by dislocation slips with limited tension twinning. As evidenced in the deformation pole figures and TVFs, the change of texture due to twinning is trivial: TVF = 2.5% at $\theta = 0^\circ$ and TVF = 13% at $\theta = 22.5\%$. For the $\theta = 45^\circ$ material orientation, the stress-strain curve displays a concave-down shape (up to $\sim 10\%$) followed by a concave-down shape. Due to the high Schmid factors (SFs) and the low CRSS values, basal slips act as the major deformation mechanism during the whole plastic deformation in this material orientation [55]. As the strain increases, tension twins gradually form, while the pyramidal < a+c> slips as well

as the basal slips are activated in twinned grains to accommodate the plastic deformation [55]. The TVF of tension twins at fracture is 62%.

When the orientation angle (θ) is larger than 45°, the stress-strain curve displays a sigmodal shape, where tension twinning plays a dominating role in the plastic deformation. The TVFs of tension twins at fracture can attain as high as 80.3% and 96%, respectively, for $\theta=67.5^{\circ}$ and 90° (ND). The transformation in the stress-strain curve from a concave-up shape in the initial stage to a later concave-down shape signifies the exhaustion of tension twinning as well as the involvement of non-basal dislocation slips [56,57]. Prismatic slips contribute significantly to the plastic deformation for the $\theta=67.5^{\circ}$ and 90° (ND) under tension at the later deformation stage [55]. The overall tendency of the stress-strain curves under tension at $\theta=0^{\circ}$, 45° and 90° is consistent with the results obtained from a rolled AZ31 Mg alloy under the same tensile directions [42].

3.2. Macroscopic fracture surface

Fig. 3 shows the macroscopic profiles of the fracture surfaces. The fracture surfaces exhibit two macroscopic features: (1) flat-surfaced shear fracture and (2) irregular-shaped brittle-like fracture. For the material orientations at $\theta=45^\circ$ and 22.5° , a flat shear surface is observed (Fig. 3). The loading axis (Z-axis) and the projected trace of the fracture surface on the YZ plane form angles of 40° and 30° for $\theta=45^\circ$ and 22.5° , respectively (Fig. 3). The macroscopic fracture surfaces under tension at $\theta=0^\circ$, 67.5° , and 90° show irregular-shaped brittle-like features composed of ridges and islands.

3.3. Fracture mechanisms

To identify the fracture mechanisms, we examined the microcracks and microstructural features in the region near the fracture surface on the YZ plane cut along the diametral direction in the cylindrical testing specimen. Specifically, short microcracks with lengths in tens of microns are used to infer the crack initiation mechanism. Intermediate-sized microcracks spanning across several grains with lengths in hundreds of microns are used to identify early-stage crack growth. For those final fracture surfaces showing flat shear plane ($\theta=22.5^{\circ}$ and 45°), we

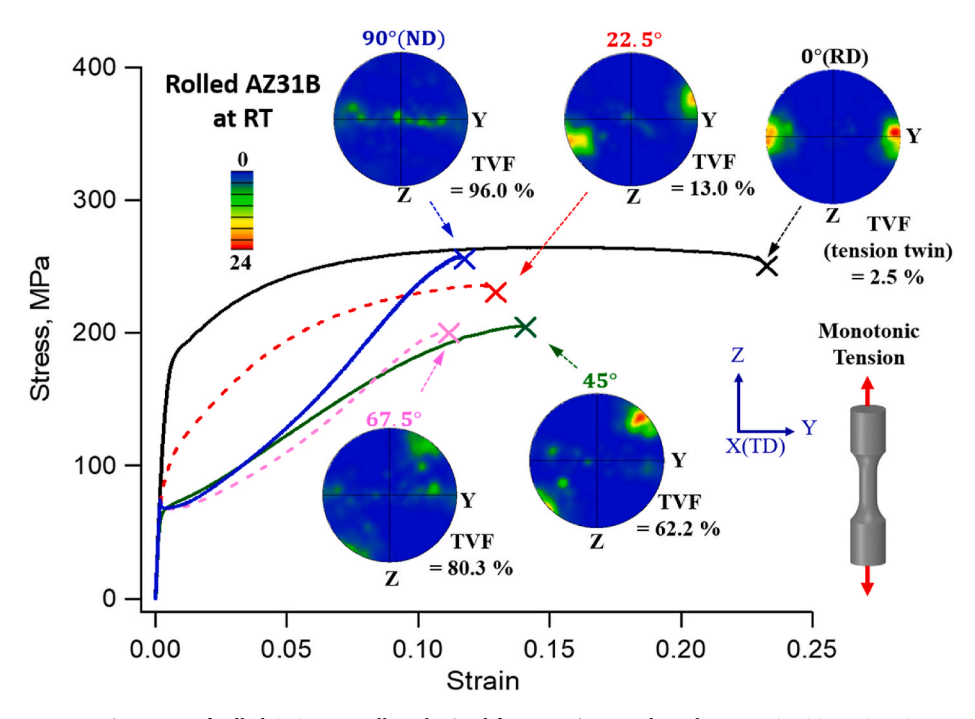


Fig. 2. Monotonic tension stress-strain curves of rolled AZ31B Mg alloy obtained from specimens taken along $\theta = 0^{\circ}$, 22.5°, 45°, 67.5° and 90° with respect to the rolled direction. The {0001} pole figures and tension twin volume fractions after tensile fracture are included in the figure.

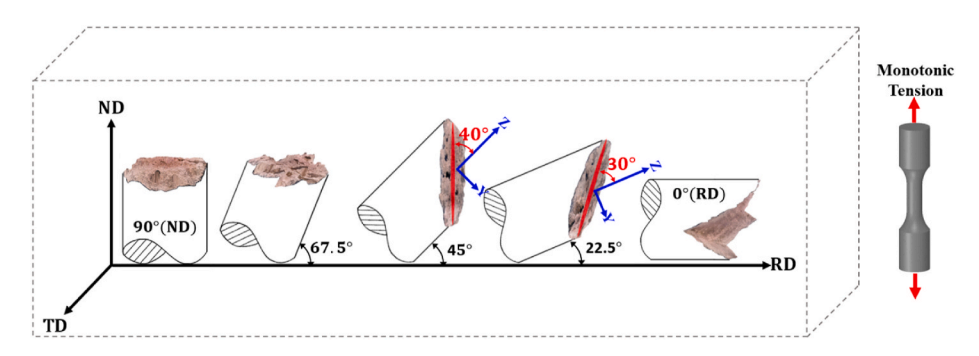


Fig. 3. Macroscopic fracture surfaces of rolled AZ31B Mg alloy tested under monotonic tension along different material orientations at $\theta = 0^{\circ}$, 22.5°, 45°, 67.5° and 90° with respect to the rolled direction.

further carried out trace analysis for the fracture surface to infer the macro-crack propagation mode.

3.3.1. Tension at $\theta = 45^{\circ}$

Fig. 4a shows the fracture surface resulted from tension at $\theta=45^\circ$. The trace of fracture surface projected on the YZ plane forms an angle, α , of 40° with respective to the Z-axis. It is noticeable that the bulk shear stress resolved on the fracture surface is close to the maximum shear stress in the uniaxial tensile stress state. Therefore, it is hypothesized that the final fracture at $\theta=45^\circ$ is proceeded by shear cracking accommodated by localized shear deformation operated via certain dislocation slip/twinning modes.

To discern a slip/twinning system responsible for the shear cracking, we characterized the grain orientations in a relatively large area near the

fracture surface on the YZ plane, which is exposed by cutting the cylindrical specimen along its diameter (Fig. 4a). We first carried out SF analysis to determine what slip/twinning systems are most likely operative. In the case of tension at $\theta=45^\circ$, basal slip is the dominant deformation mechanism due to its extremely low CRSS and their high SF values, most of which is higher than 0.3 (Fig. 4b). We further plot all the traces corresponding to the basal plane by projecting the basal plane at every crystal orientation onto the YZ plane. By comparing the histogram of the orientation (β) of the basal-plane traces with the orientation (α) of the fracture-surface trace (Fig. 4b), we find that the basal-slip plane traces match well with that of the fracture surface, which indicates shear cracking is accommodated by basal slips. In fact, we have ruled out other less active slip/twinning systems, including prismatic slip, pyramidal $<\alpha+c>$ slip, tension twinning and compression twining. None of them

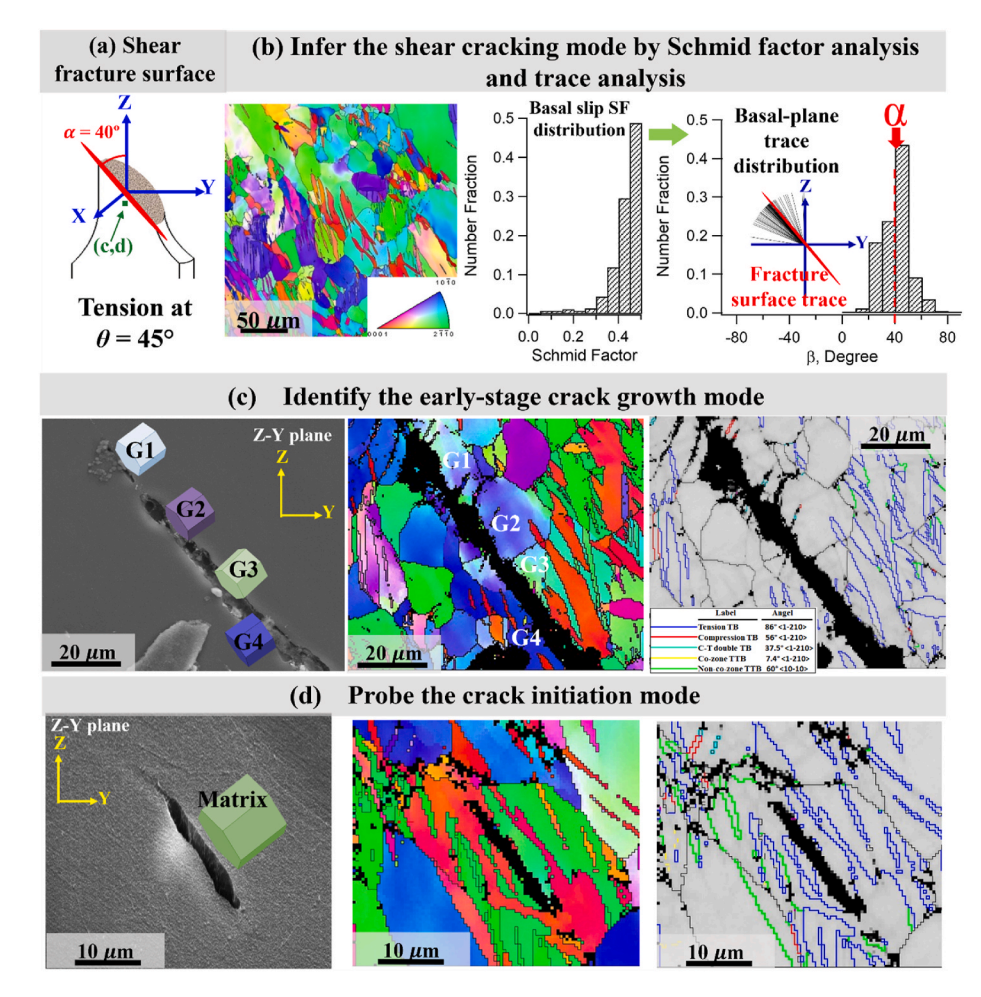


Fig. 4. Fracture mechanisms under tension at $\theta =$ 45°. (a) Trace of shear fracture surface forming orientation angles of $\alpha = 40^{\circ}$ to the Z-axis on the YZ plane. (b) Inference of shear cracking mode by Schmid factor analysis and trace analysis of the shear fracture surface. (c) Probing of the crack initiation mode by characterizing the microcrack. (d) Identification of the early-stage crack growth mode by characterizing intermediate-sized microcrack. The left, middle, and right images in (c,d) are SEM micrograph, inverse pole figure (IPF) map and image quality (IQ) map, respectively. In the IQ map, grain boundaries are denoted by black lines. Tension, compression, and T-C double twin boundaries are colored in blue, red, and light blue respectively. Co-zone and none co-zone twin-twin boundaries are delineated in yellow and green colors. (For interpretation of the references to color in this figure legend, the reader is referred to the Web version of this article.)

shows a good agreement of the slip/twin plane traces with the fracture surface trace.

To clarify the crack initiation mode, we characterized the microstructure in the vicinity of short microcracks sized in tens of microns. Fig. 4c shows a short microcrack sized approximately 20 μm observed in a single grain. As viewed in the IPF and IQ maps, pronounced tension twins are developed in the grain. However, it is interesting to find that the microcrack persistently resides on the basal-slip plane of the matrix area in the grain. Our observation in Fig. 4c indicates that crack initiation under tension at $\theta=45^\circ$ might originate from the local damages induced by impingement of tension twins on the basal slip bands.

To further elucidate the crack propagation mode, in particular during the early-growth stage, we characterized the microstructure in the vicinity of intermediate-sized microcrack which spans across several grains, as shown in Fig. 4d. It is revealed that the microcrack (inclined $\sim\!40^\circ$ to the Z-axis) propagates in transgranular mode through grain G1 and grain G2. The propagation route is followed by intergranular cracking on grain boundary (GB) formed between grain G3 and grain G4. This result indicates that the early-stage crack growth is actually proceeded by alternative routes via transgranular cracking along the basal-slip planes and intergranular cracking at GBs.

3.3.2. Tension at $\theta = 22.5^{\circ}$

The fracture surface under tension at $\theta=22.5^\circ$ shows similar flat shear plane to that of $\theta=45^\circ$ (Fig. 5a). However, the trace of the fracture surface forms an angle of 30° to the Z-axis on the YZ plane. Therefore, we applied the same procedures using Schmid analysis and trace analysis to infer the cracking mechanism. As shown in Fig. 5b, the trace of

the fracture surface matches well with the basal-slip plane, implying that cracking is mainly driven by the shear deformation localized in basal slip bands.

When we further examine the small microcrack within one grain (Fig. 5c), compression twins and C-T double twins are clearly developed in connection to the microcrack. However, it is interesting to find that the habit plane of the microcrack is persistently the basal plane. We conclude that the microcrack observed on the basal slip band in Fig. 5c is likely nucleated from the local damage induced by the impingement of compression and/or double twinning. This is unlike the case of tension at $\theta=45^\circ$ (Fig. 4c), where cracking in the basal slip band is likely to be nucleated from the impingement damage by twinning. The observation of compression and C-T double twins in Fig. 5c is reasonable as tension at $\theta=22.5^\circ$ leads to a higher favorability of compression twin and C-T double twinning than tension at $\theta=45^\circ$.

In Fig. 5d, we examine the microcrack size in lengths spanning from several grains (Fig. 5d). The crack propagation path persistently aligns well with the basal slip traces, confirming that the crack extension is dominated by cracking along basal slip bands. Similar to the case of tension at $\theta=45^{\circ}$ (Fig. 4c), GB cracking can be found in the propagation route of the microcrack. Moreover, more compression twins and C-T double twins are found in the vicinity of microcrack (see the red and light blue TBs in the image quality map in Fig. 5c).

3.3.3. Tension at $\theta = 0^{\circ}$ (RD)

Different from the cases of tension at $\theta=45^{\circ}$ and 22.5° , tension at $\theta=0^{\circ}$ (RD), 67.5° and 90° (ND) exhibits brittle fracture surfaces showing irregular-shaped ridge and island features (Fig. 3). As a result, the trace

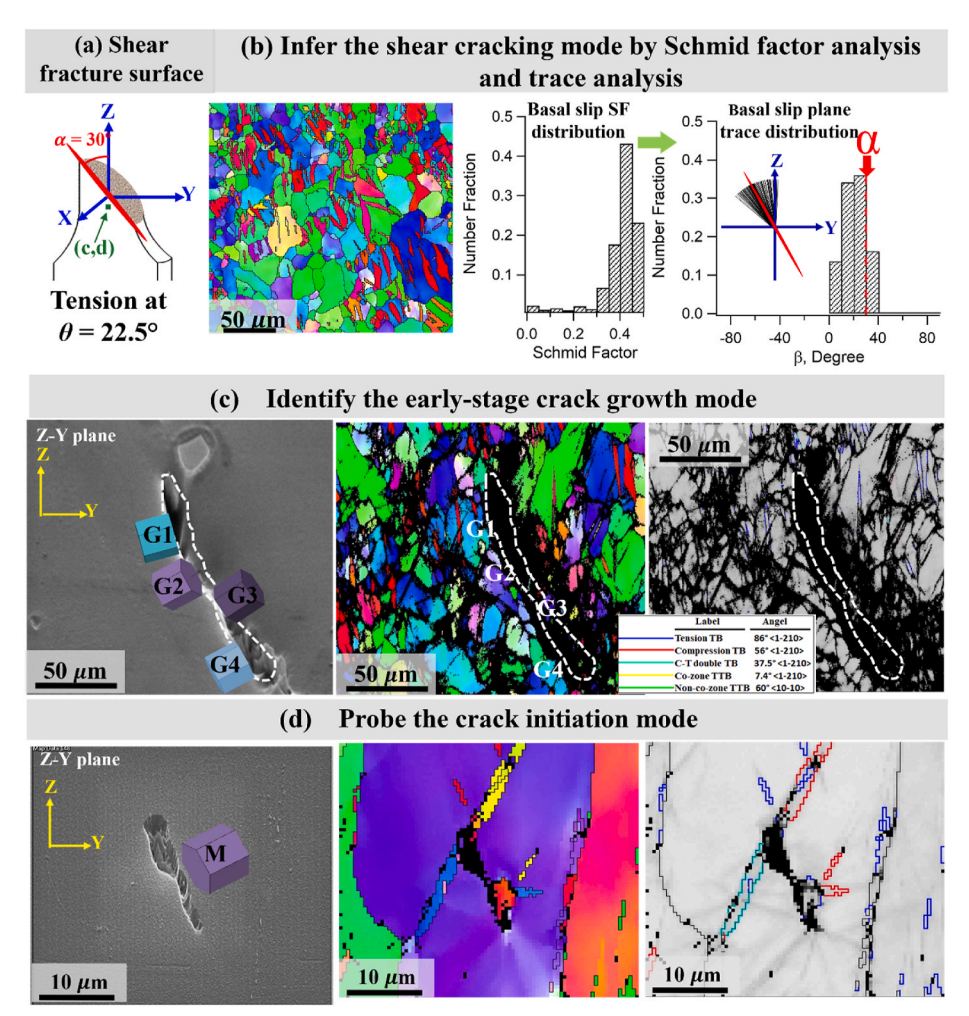


Fig. 5. Fracture mechanisms under tension at $\theta =$ 22.5°. (a) Trace of shear fracture surface forming orientation angles of $\alpha=30^\circ$ to the Z-axis on the YZ plane. (b) Inference of the shear cracking mode by Schmid factor analysis and trace analysis of the shear fracture surface. (c) Probing the crack initiation mode by characterizing the short microcrack. (d) Identification of the early-stage crack growth mode by characterizing intermediate-sized microcrack. The left, middle, and right images in (c,d) are SEM micrograph, inverse pole figure (IPF) map and image quality (IQ) map, respectively. In the IQ map, grain boundaries are denoted by black lines. Tension, compression, and double C-T twin boundaries are colored in blue, red, and light blue respectively. Co-zone and none co-zone twin-twin boundaries are delineated in yellow and green colors. (For interpretation of the references to color in this figure legend, the reader is referred to the Web version of this article.)

analysis cannot be applied to the fracture surface for inferring the crack propagation mode. However, we can still characterize the microcrack in the local area near (within a distance of ~ 0.5 mm) the fracture surface to investigate the early-stage crack growth mode as well as the crack initiation mechanism.

Fig. 6 shows the SEM and EBSD characterization area near the fracture surface on the YZ plane. Fig. 6b and c presents two microcracks located beneath the fracture surface, both of which are sized approximately 12 µm in length. These microcracks appear to be of lenticular shape and have sharp crack tips. This microcrack morphology is likely to result from TB cracking [42,58]. EBSD characterization of the microstructure surrounding the microcrack reveals clear development of compression twins and C-T double twins. In Grain A (Fig. 6b), a double twin trace shows the same alignment with the microcrack. This indicates the microcrack in Grain A is likely a result of TB cracking by the same C-T double twin variant. Similarly, a compression twin (C5) along with a connected double twin C5-T1 are found in the vicinity of a microcrack in Grain B (Fig. 6c). Although there is no direct connection between the occurrence of a microcrack and compression/double twins, the large local shear by compression and C-T double twinning may result in incompatible deformation and may potentially lead to initiation of microcracks. In fact, the results evidenced in our work under tension at $\theta = 0^{\circ}$ (RD) are consistent with those regularly reported in prior studies, confirming that the detrimental role of compression/double twinning on crack initiation [50-54].

3.3.4. Tension at $\theta = 90^{\circ}$ (ND) and 67.5°

As shown in Fig. 3, the fracture surfaces obtained from tension at $\theta=90^\circ$ (ND) and 67.5° share similar brittle-like features as that under tension at $\theta=0^\circ$. This macroscopic fracture feature is consistent with the observation from a previous study on the same material that a serrated brittle-like fracture surface is exhibited under tension along the ND [42]. However, as discussed in Section 3.1, pronounced tension twins are developed after tensile fracture. The TVFs after fracture attain as high as 80.3% and 96% for $\theta=67.5^\circ$ and 90° (ND), respectively. It would be interesting to see whether the fracture mechanisms, in particular the crack initiation mode, are still ascribed to double-twinning induced damage.

Fig. 7 shows the microcracks characterized in the local area near the fracture surface for tension at $\theta=90^\circ$ (ND) and 67.5°. Unlike the predominant lenticular-shaped microcracks due to TB cracking under tension at $\theta=0^\circ$, the microcracks developed in tension at $\theta=90^\circ$ (ND) and 67.5° are much shorter in length spanning only $\sim\!5\text{--}20~\mu\text{m}$ (see the SEM

images in Fig. 7b and d) and show relatively blunted crack tips. Further EBSD characterization reveals that the short microcracks are located at triple joints and grain boundaries. For instance, under tension $\theta = 90^{\circ}$ (ND) (Fig. 7b), the microcrack is developed mainly at the GB between grain G2 and grain G3 where a triple joint met by grains G1, G2, and G3 is adjoined. The misorientation angles between the neighboring grains are 59°, 58°, and 88° for G1-G2 pair, G2 and G3 pair, G3-G1 pair, respectively. This indicates that the GB cracking is favorable to be initiated from the high angle grain boundaries (HAGBs). Interestingly, significant none co-zone twin-twin boundaries (TTBs) are developed in G2 and G3 due to the coalescence of fully-expanded tension twins. Moreover, a tension-compression-tension (T-C-T) tertiary twin is observed in G3 with its tip connected to the microcrack. These observations shed lights that the GB impingement of dislocations from the formation of both none co-zone TTBs and T-C-T tertiary twins can lead to local stress concentration, causing twinning-induced GB damage and triggering GB cracking subsequently. As shown in Fig. 7d, the microcrack found in tension at $\theta = 67.5^{\circ}$ is also resulted from GB cracking at the high angle grain boundaries where a triple joint is detected. Likewise, the none co-zone TTBs are frequently connected to the microcrack and considered as the major driving force for GB cracking.

4. Further discussion

C-T double twins are commonly considered as a detrimental factor that causes the microcrack nucleation that leads to final failure [50–54]. Such an understanding reflects one facet of the anisotropic nature of fracture in wrought Mg materials. In fact, double twinning, as a critical fracture mechanism, is typically observed in experiments where tensile loading is unfavorable for extensive tension twinning. The contribution of the current work is to uncover a more comprehensive picture of the tensile fracture behavior in wrought Mg alloy. The major findings are summarized in Fig. 8. The final fracture modes are closely related to the deformation modes operated under a specific stress state. Basically, two fracture modes are categorized: (1) shear cracking which results in flat macroscopic shear fracture surface under tension at $\theta=45^\circ$ and 22.5°; and (2) brittle-like cracking which leads to irregular-shaped fracture surface under tension at $\theta=0^\circ$, 67.5, and 90°.

As shown in Fig. 8a and b, shear cracking occurring under tension at $\theta=45^\circ$ and 22.5° is mainly resulted from the extensive shear deformation accommodated by basal slips which are the dominant deformation modes in these two loading directions. Cracks are nucleated solely from basal slip bands at local damages induced by impingement of

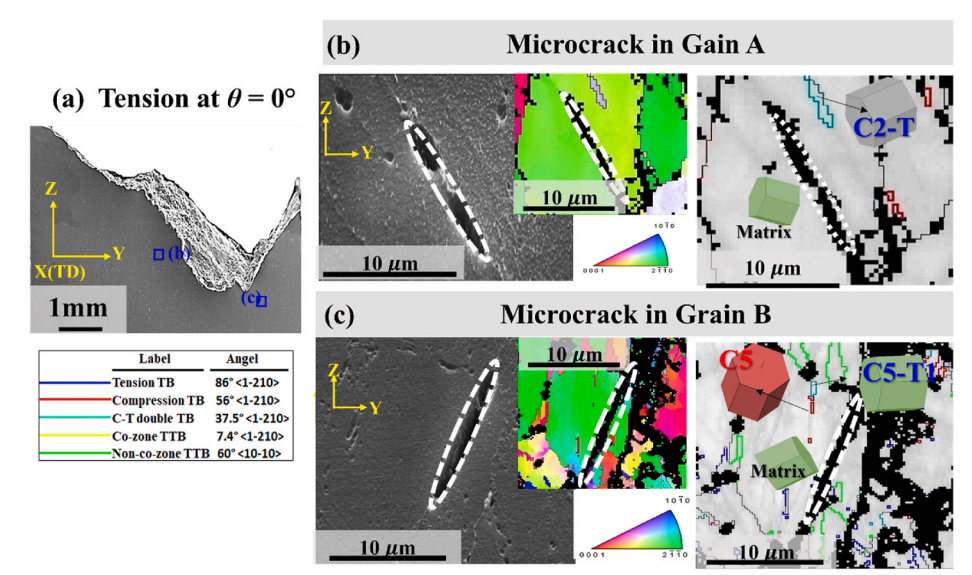


Fig. 6. Microcracks observed for the 0° (RD) specimen under tension: (a) SEM image captured in the area near the fracture surface on the YZ plane, which is sectioned by cutting the cylindrical specimen through its diameter. (b,c) SEM image along with EBSD results (IPF and IQ maps) showing the microstructural features surrounding the microcracks. In the IQ map, grain boundaries are denoted by black lines. Tension, compression, and C-T double twin boundaries are colored in blue, red, and light blue respectively. Co-zone and none co-zone twin-twin boundaries are delineated in yellow and green colors. (For interpretation of the references to color in this figure legend, the reader is referred to the Web version of this article.)

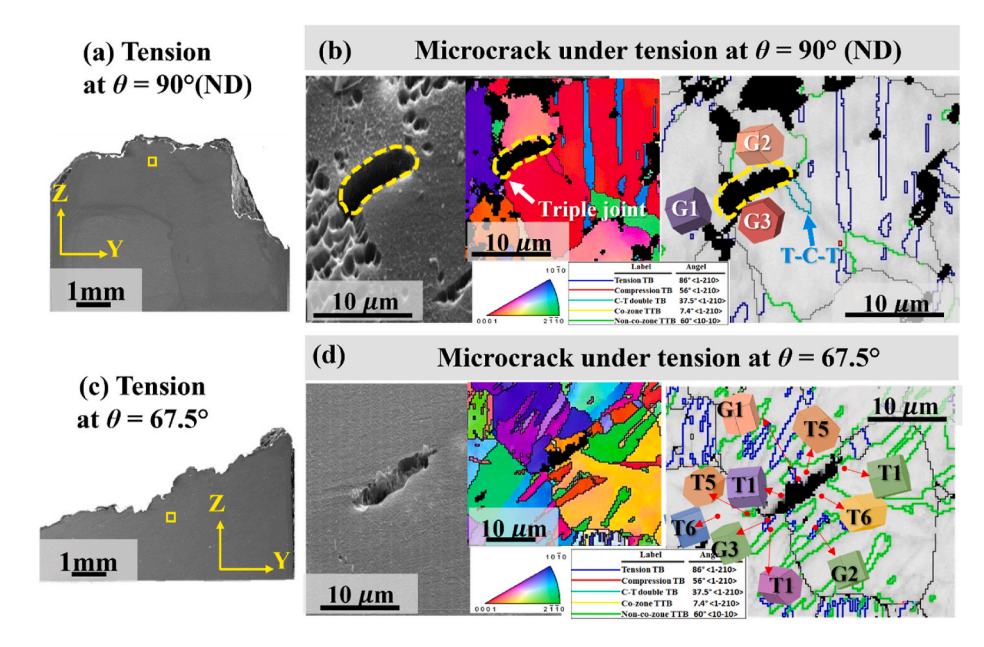


Fig. 7. Microcracks observed on the specimens subjected to tension at $\theta = 90^{\circ}$ (ND) and 67.5°: (a,c) SEM image captured in the area near the fracture surface on the YZ plane which is sectioned by cutting the cylindrical specimen through the diameter. (b,d) SEM image and EBSD results (IPF and IQ maps) showing the microstructural features surrounding the microcracks. In the IQ map, grain boundaries are denoted by black lines. Tension, compression, and C-T double twin boundaries are colored in blue, red, and light blue respectively. Cozone and none co-zone twin-twin boundaries are delineated in yellow and green colors. (For interpretation of the references to color in this figure legend, the reader is referred to the Web version of this article.)

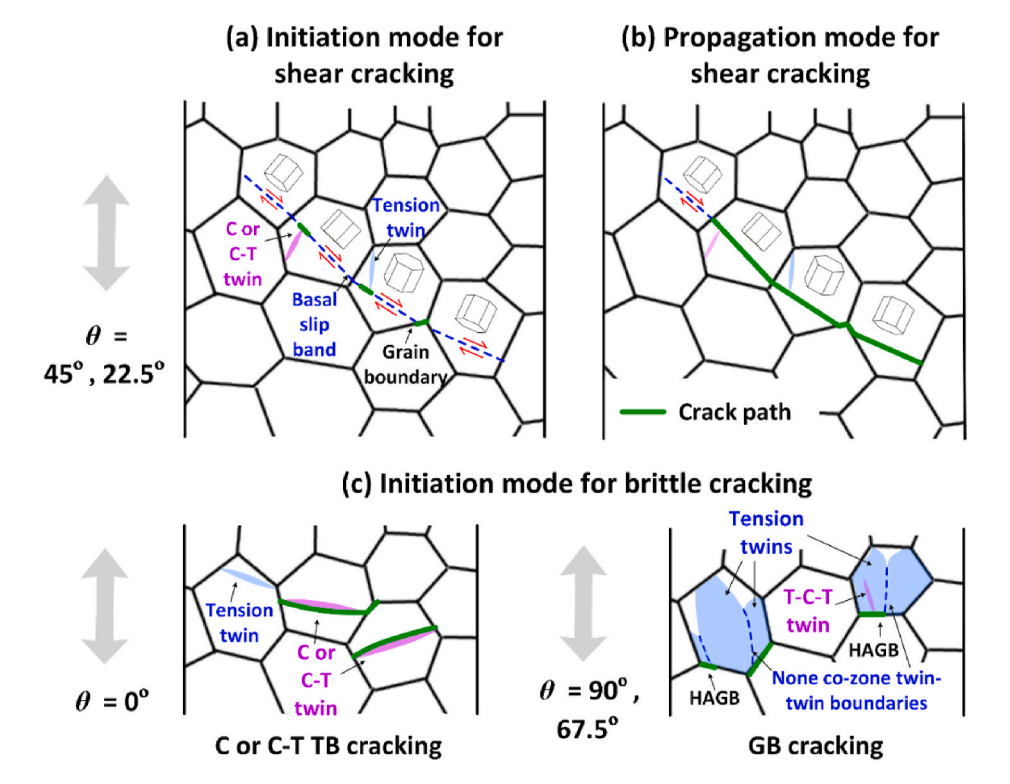


Fig. 8. Schematics summarizing the anisotropic fracture mechanisms in rolled Mg alloy. (a) Initiation mode for shear cracking in tension at $\theta=45^{\circ}$ and 22.5°. (b) Crack propagation mode for shear cracking in tension at $\theta=45^{\circ}$ and 22.5°. (c) Initiation mode for brittle-like cracking in tension at $\theta=0^{\circ}$, 67.5, and 90°. "C or C-T TB" represents "compression or compression-tension twin boundary". "HAGB" denotes "high-angle grain boundary".

tension, compression, and C-T double twins (Fig. 8a). Due to the strong basal texture, basal slips under tension at $\theta=45^\circ$, 22.5° can be easily transmitted across neighboring grains, most of which have low misorientation angles. The propagation of the nucleated crack, which is driven by the shear deformation localized in basal-slip bands, follows the transmitted basal-slip bands across the neighboring grains (Fig. 8b). As a result, the final crack follows a preferential path on the YZ plane whose orientation matches well with that of the basal-plane traces projected on the same observation plane, as characterized in Figs. 4 and 5.

The macroscopic fracture surfaces under tension at $\theta = 0^{\circ}$, 67.5, and

 90° show brittle-like features with irregular-shaped ridges and islands. Since there is no preferential crack propagation path, we only focus on the crack initiation modes by charactering microcracks near the fracture surface to reveal the fracture mechanisms in these material orientations. As shown in Fig. 8c, crack initiation mode displays distinctive microstructural origins between the case of $\theta=0^{\circ}$ and the cases of $\theta=90^{\circ}$ and 67.5° . For $\theta=0^{\circ}$, where tension twinning is unfavored and compression twinning is promoted, crack initiation is commonly detected as cracking at compression and/or C-T double twin boundaries. However, tension at $\theta=90^{\circ}$ and 67.5° favors extensive tension twinning, which often results

in significant twin-twin interaction and even the development of T-C-T tertiary twins. Rather than TB cracking, cracking at high-angle grain boundaries (HAGBs) acts as the dominant crack initiation mode at $\theta =$ 90° and 67.5°. Interestingly, C-T-C tertiary twins and none co-zone TTBs with high-angle misorientation are found to be connected to the crack initiation sites, suggesting that the deformation incompatibility induced by the development of these microstructures may serve as the driving force for crack initiation at $\theta = 90^{\circ}$ and 67.5° . It is worth noting that microcracks nucleated by either TB cracking at $\theta=0^\circ$ or GB cracking at $\theta=90^{\circ}$ and 67.5° are sparsely distributed at multiple locations in the material. Unlike the cases of tension at $\theta = 45^{\circ}$ and 22.5° , there is no preferential crack propagation route for the nucleated microcracks to grow probably due to the large difference in the orientation of these microcracks (see Figs. 6 and 7). That is also the reason why the final fracture surface shows brittle-like features with irregular-shaped ridges and islands.

5. Conclusions

An experimental study of the anisotropic fracture behavior of a rolled AZ31B magnesium alloy was carried out with monotonic tension in five material orientations. θ denotes the angle between the axial direction of the tension testing specimen and the rolled direction of the material. Major conclusions are drawn as follows.

- 1. The material orientation affects the fracture behavior. Tension at $\theta=0^\circ$, 67.5°, and 90° results in brittle-like fracture surfaces while tension at $\theta=45^\circ$ and 22.5° displays macroscopic shear fracture behavior.
- 2. Crack initiation under tension at $\theta=45^\circ$ and 22.5° is originated from shear deformation in the basal slip bands at local damages induced by impingement of tension, compression and/or compression-tension twins. Crack extension is driven by localized shear deformation in basal slip bands which can be transmitted across neighboring grains, resulting in a final crack path following basal plane traces.
- 3. The microstructural origins of brittle-like cracking are different between the case of tension at $\theta=0^\circ$ and that of tension at $\theta=67.5^\circ$ and 90° . Twin boundary cracking in compression and/or compression-tension double twins is commonly detected in tension at $\theta=0^\circ$ whereas high-angle grain boundary cracking, which is facilitated by the impingements of tension-compression-tension tertiary twins and the none co-zone twin-twin boundaries, acts as the crack initiation mode in tension at $\theta=67.5^\circ$ and 90° .

Data availability

The raw/processed data required to reproduce these findings cannot be shared at this time due to technical or time limitations.

CRediT authorship contribution statement

Yuqian Wang: Data curation, Formal analysis, Writing – original draft, Writing – review & editing. **Qin Yu:** Formal analysis, Writing – original draft, Writing – review & editing. **Yanyao Jiang:** Data curation, Funding acquisition, Supervision, Validation, Writing – original draft, Writing – review & editing.

Declaration of competing interest

The authors declare that they have no known competing financial interests or personal relationships that could have appeared to influence the work reported in this paper.

Acknowledgments

The research was supported by the U.S. National Science Foundation (CMMI-1762312).

References

- D.S. Mehta, S.H. Masood, W.Q. Song, Investigation of wear properties of magnesium and aluminum alloys for automotive applications, J. Mater. Process. Technol. (2004), https://doi.org/10.1016/j.jmatprotec.2004.04.247.
- [2] M.P. Staiger, A.M. Pietak, J. Huadmai, G. Dias, Magnesium and its alloys as orthopedic biomaterials: a review, Biomaterials 27 (2006) 1728–1734, https://doi. org/10.1016/j.biomaterials.2005.10.003.
- [3] L.Y. Chen, J.Q. Xu, H. Choi, M. Pozuelo, X. Ma, S. Bhowmick, J.M. Yang, S. Mathaudhu, X.C. Li, Processing and properties of magnesium containing a dense uniform dispersion of nanoparticles, Nature 528 (2015) 539–543, https://doi.org/ 10.1038/nature16445
- [4] W.S. Miller, L. Zhuang, J. Bottema, A.J. Wittebrood, P. De Smet, A. Haszler, A. Vieregge, Recent development in aluminium alloys for the automotive industry, Mater. Sci. Eng. 280 (2000) 37–49, https://doi.org/10.1016/S0921-5093(99) 00653-X.
- [5] M.K. Kulekci, Magnesium and its alloys applications in automotive industry, Int. J. Adv. Manuf. Technol. 39 (2008) 851–865, https://doi.org/10.1007/s00170-007-1279-2
- [6] A. Heinz, A. Haszler, C. Keidel, S. Moldenhauer, R. Benedictus, W.S. Miller, Recent development in aluminium alloys for aerospace applications, Mater. Sci. Eng. 280 (2000) 102–107, https://doi.org/10.1016/S0921-5093(99)00674-7.
- [7] T.M. Pollock, Weight loss with magnesium alloys, Science 328 (2010) 986–987, https://doi.org/10.1126/science.1182848, 80-.
- [8] F. Wang, S. Sandlöbes, M. Diehl, L. Sharma, F. Roters, D. Raabe, In situ observation of collective grain-scale mechanics in Mg and Mg-rare earth alloys, Acta Mater. 80 (2014) 77–93, https://doi.org/10.1016/j.actamat.2014.07.048.
- [9] D. Hou, T. Liu, H. Chen, D. Shi, C. Ran, F. Pan, Analysis of the microstructure and deformation mechanisms by compression along normal direction in a rolled AZ31 magnesium alloy, Mater. Sci. Eng. 660 (2016) 102–107, https://doi.org/10.1016/j. msea.2016.02.020.
- [10] C. Guo, R. Xin, C. Ding, B. Song, Q. Liu, Understanding of variant selection and twin patterns in compressed Mg alloy sheets via combined analysis of Schmid factor and strain compatibility factor, Mater. Sci. Eng. 609 (2014) 92–101, https:// doi.org/10.1016/i.msea.2014.04.103.
- [11] H. Yu, C. Li, Y. Xin, A. Chapuis, X. Huang, Q. Liu, The mechanism for the high dependence of the Hall-Petch slope for twinning/slip on texture in Mg alloys, Acta Mater. 128 (2017) 313–326, https://doi.org/10.1016/j.actamat.2017.02.044.
- [12] Z.Z. Shi, X.F. Liu, Characteristics of cross grain boundary contraction twin pairs and bands in a deformed Mg alloy, J. Alloys Compd. 692 (2017) 274–279, https:// doi.org/10.1016/j.jallcom.2016.09.024.
- [13] N.V. Dudamell, I. Ulacia, F. Gálvez, S. Yi, J. Bohlen, D. Letzig, I. Hurtado, M. T. Pérez-Prado, Twinning and grain subdivision during dynamic deformation of a Mg AZ31 sheet alloy at room temperature, Acta Mater. 59 (2011) 6949–6962, https://doi.org/10.1016/j.actamat.2011.07.047.
- [14] M. Hou, H. Zhang, J. Fan, Q. Zhang, L. Wang, H. Dong, B. Xu, Microstructure evolution and deformation behaviors of AZ31 Mg alloy with different grain orientation during uniaxial compression, J. Alloys Compd. 741 (2018) 514–526, https://doi.org/10.1016/j.iallcom.2017.12.312.
- [15] H. Wang, C.J. Boehlert, Q.D. Wang, D.D. Yin, W.J. Ding, In-situ analysis of the tensile deformation modes and anisotropy of extruded Mg-10Gd-3Y-0.5Zr (wt.%) at elevated temperatures, Int. J. Plast. 84 (2016) 255–276, https://doi.org/ 10.1016/j.ijplas.2016.06.001.
- [16] C.J. Boehlert, Z. Chen, I. Gutiérrez-Urrutia, J. Llorca, M.T. Pérez-Prado, In situ analysis of the tensile and tensile-creep deformation mechanisms in rolled AZ31, Acta Mater. 60 (2012) 1889–1904, https://doi.org/10.1016/j. octamet 2011.0.035
- [17] A. Chakkedath, T. Maiti, J. Bohlen, S. Yi, D. Letzig, P. Eisenlohr, C.J. Boehlert, Contraction twinning dominated tensile deformation and subsequent fracture in extruded Mg-1Mn (wt pct) at ambient temperature, Metall. Mater. Trans. A Phys. Metall. Mater. Sci. 49 (2018) 2441–2454, https://doi.org/10.1007/s11661-018-4557-8
- [18] B. Song, R. Xin, G. Chen, X. Zhang, Q. Liu, Improving tensile and compressive properties of magnesium alloy plates by pre-cold rolling, Scripta Mater. 66 (2012) 1061–1064, https://doi.org/10.1016/j.scriptamat.2012.02.047.
- [19] S. Niknejad, S. Esmaeili, N.Y. Zhou, The role of double twinning on transgranular fracture in magnesium AZ61 in a localized stress field, Acta Mater. 102 (2016) 1–16, https://doi.org/10.1016/j.actamat.2015.09.026.
- [20] J. Koike, R. Ohyama, Geometrical criterion for the activation of prismatic slip in AZ61 Mg alloy sheets deformed at room temperature, Acta Mater. 53 (2005) 1963–1972, https://doi.org/10.1016/j.actamat.2005.01.008.
- [21] X.Y. Lou, M. Li, R.K. Boger, S.R. Agnew, R.H. Wagoner, Hardening evolution of AZ31B Mg sheet, Int. J. Plast. 23 (2007) 44–86, https://doi.org/10.1016/j. iiples 2006.03.005
- [22] S.H. Park, S.G. Hong, W. Bang, C.S. Lee, Effect of anisotropy on the low-cycle fatigue behavior of rolled AZ31 magnesium alloy, Mater. Sci. Eng. 527 (2010) 417–423, https://doi.org/10.1016/j.msea.2009.08.044.

- [23] S. Begum, D.L. Chen, S. Xu, A.A. Luo, Effect of strain ratio and strain rate on low cycle fatigue behavior of AZ31 wrought magnesium alloy, Mater. Sci. Eng. 517 (2009) 334–343, https://doi.org/10.1016/j.msea.2009.04.051.
- [24] J. Albinmousa, H. Jahed, S. Lambert, Cyclic behaviour of wrought magnesium alloy under multiaxial load, Int. J. Fatig. 33 (2011) 1127–1139, https://doi.org/ 10.1016/j.ijfatigue.2011.01.009.
- [25] D. Hou, T. Liu, L. Luo, L. Lu, H. Chen, D. Shi, Twinning behaviors of a rolled AZ31 magnesium alloy under multidirectional loading, Mater. Char. 124 (2017) 122–128, https://doi.org/10.1016/j.matchar.2016.11.046.
- [26] Y. Xiong, Q. Yu, Y. Jiang, Multiaxial fatigue of extruded AZ31B magnesium alloy, Mater. Sci. Eng. 546 (2012) 119–128, https://doi.org/10.1016/j. mseq. 2012.03.039
- [27] F. Yang, S.M. Yin, S.X. Li, Z.F. Zhang, Crack initiation mechanism of extruded AZ31 magnesium alloy in the very high cycle fatigue regime, Mater. Sci. Eng. 491 (2008) 131–136. https://doi.org/10.1016/j.msea.2008.02.003
- [28] S.G. Hong, S. Hyuk Park, Y.H. Huh, C. Soo Lee, Anisotropic fatigue behavior of rolled Mg-3AI-1Zn alloy, J. Mater. Res. 25 (2010) 966–971, https://doi.org/ 10.1557/imr.2010.0123
- [29] Y.J. Wu, R. Zhu, J.T. Wang, W.Q. Ji, Role of twinning and slip in cyclic deformation of extruded Mg-3%Al-1%Zn alloys, Scripta Mater. 63 (2010) 1077–1080, https:// doi.org/10.1016/j.scriptamat.2010.08.008.
- [30] F. Lv, F. Yang, Q.Q. Duan, Y.S. Yang, S.D. Wu, S.X. Li, Z.F. Zhang, Fatigue properties of rolled magnesium alloy (AZ31) sheet: influence of specimen orientation, Int. J. Fatig. 33 (2011) 672–682, https://doi.org/10.1016/j.iifsting.2010.10.103.
- [31] A.A. Roostaei, H. Jahed, Role of loading direction on cyclic behaviour characteristics of AM30 extrusion and its fatigue damage modelling, Mater. Sci. Eng. 670 (2016) 26–40, https://doi.org/10.1016/j.msea.2016.05.116.
- [32] Y. Xiong, Q. Yu, Y. Jiang, Cyclic deformation and fatigue of extruded AZ31B magnesium alloy under different strain ratios, Mater. Sci. Eng. 649 (2016) 93–103, https://doi.org/10.1016/j.msea.2015.09.084.
- [33] S.H. Park, S.G. Hong, J. Yoon, C.S. Lee, Influence of loading direction on the anisotropic fatigue properties of rolled magnesium alloy, Int. J. Fatig. 87 (2016) 210–215, https://doi.org/10.1016/j.ijfatigue.2016.01.026.
- [34] J.B. Jordon, H.R. Brown, H. El Kadiri, H.M. Kistler, R.L. Lett, J.C. Baird, A.A. Luo, Investigation of fatigue anisotropy in an extruded magnesium alloy, Int. J. Fatig. 51 (2013) 8–14, https://doi.org/10.1016/j.ijfatigue.2013.01.006.
- [35] S. Ishihara, S. Taneguchi, H. Shibata, T. Goshima, A. Saiki, Anisotropy of the fatigue behavior of extruded and rolled magnesium alloys, Int. J. Fatig. 50 (2013) 94–100. https://doi.org/10.1016/j.jifatigue.2012.02.011.
- [36] L. Wu, S.R. Agnew, Y. Ren, D.W. Brown, B. Clausen, G.M. Stoica, H.R. Wenk, P. K. Liaw, The effects of texture and extension twinning on the low-cycle fatigue behavior of a rolled magnesium alloy, AZ31B, Mater. Sci. Eng. A. 527 (2010) 7057–7067, https://doi.org/10.1016/j.msea.2010.07.047.
- [37] C. Wang, T.J. Luo, J.X. Zhou, Y.S. Yang, Anisotropic cyclic deformation behavior of extruded ZA81M magnesium alloy, Int. J. Fatig. 96 (2017) 178–184, https://doi. org/10.1016/j.jifatigue.2016.11.020.
- [38] S.M. Yin, F. Yang, X.M. Yang, S.D. Wu, S.X. Li, G.Y. Li, The role of twinning-detwinning on fatigue fracture morphology of Mg-3%Al-1%Zn alloy, Mater. Sci. Eng. 494 (2008) 397–400, https://doi.org/10.1016/j.msea.2008.04.056.
- [39] M. Huppmann, M. Lentz, K. Brömmelhoff, W. Reimers, Fatigue properties of the hot extruded magnesium alloy AZ31, Mater. Sci. Eng. 527 (2010) 5514–5521, https://doi.org/10.1016/j.msea.2010.05.036.
- [40] Y. Xiong, X. Gong, Y. Jiang, Effect of initial texture on fatigue properties of extruded ZK60 magnesium alloy, Fatig. Fract. Eng. Mater. Struct. 41 (2018) 1504–1513, https://doi.org/10.1111/ffe.12792.
- [41] Y. Xiong, Y. Jiang, Cyclic deformation and fatigue of rolled AZ80 magnesium alloy along different material orientations, Mater. Sci. Eng. 677 (2016) 58–67, https:// doi.org/10.1016/j.msea.2016.09.031.

- [42] P. Liu, Y.C. Xin, Q. Liu, Plastic anisotropy and fracture behavior of AZ31 magnesium alloy, Trans. Nonferrous Met. Soc. China English Ed. 21 (2011) 880-884
- [43] T.S. Srivatsan, S. Vasudevan, M. Petraroli, The tensile deformation and fracture behavior of a magnesium alloy, J. Alloys Compd. 461 (2008) 154–159, https://doi. org/10.1016/j.jallcom.2007.07.061.
- [44] Y.Z. Lit, Q.D. Wang, W.J. Ding, X.Q. Zeng, Y.P. Zhu, Fracture behavior of AZ91 magnesium alloy, Mater. Lett. 44 (2000) 265–268, https://doi.org/10.1016/S0167-577X(00)00041-0.
- [45] N.S. Prasad, N. Naveen Kumar, R. Narasimhan, S. Suwas, Fracture behavior of magnesium alloys - role of tensile twinning, Acta Mater. 94 (2015) 281–293, https://doi.org/10.1016/j.actamat.2015.04.054.
- [46] J. Kang, D.S. Wilkinson, R.K. Mishra, J.D. Embury, E. Essadiqi, A. Javaid, Microstructural aspects of damage and fracture in AZ31 sheet materials, J. Mater. Eng. Perform. 22 (2013) 1386–1395, https://doi.org/10.1007/s11665-012-0399-
- [47] M.J. Nemcko, D.S. Wilkinson, On the damage and fracture of commercially pure magnesium using x-ray microtomography, Mater. Sci. Eng. 676 (2016) 146–155, https://doi.org/10.1016/j.msea.2016.08.095.
- [48] S.H.M. Azghandi, M. Weiss, B.D. Arhatari, J. Adrien, E. Maire, M.R. Barnett, A rationale for the influence of grain size on failure of magnesium alloy AZ31: an in situ X-ray microtomography study, Acta Mater. 200 (2020) 619–631, https://doi. org/10.1016/j.actamat.2020.09.016.
- [49] Q. Ma, H. El Kadiri, A.L. Oppedal, J.C. Baird, M.F. Horstemeyer, M. Cherkaoui, Twinning and double twinning upon compression of prismatic textures in an AM30 magnesium alloy, Scripta Mater. 64 (2011) 813–816, https://doi.org/10.1016/j. scriptamat.2011.01.003.
- [50] T. Al-Samman, G. Gottstein, Room temperature formability of a magnesium AZ31 alloy: examining the role of texture on the deformation mechanisms, Mater. Sci. Eng. 488 (2008) 406–414, https://doi.org/10.1016/j.msea.2007.11.056.
- [51] D. Ando, J. Koike, Y. Sutou, Relationship between deformation twinning and surface step formation in AZ31 magnesium alloys, Acta Mater. 58 (2010) 4316–4324, https://doi.org/10.1016/j.actamat.2010.03.044.
- [52] M.R. Barnett, Twinning and the ductility of magnesium alloys. Part I: "Tension" twins, Mater. Sci. Eng. 464 (2007) 1–7, https://doi.org/10.1016/j. msea.2006.12.037.
- [53] M. Lentz, M. Risse, N. Schaefer, W. Reimers, I.J. Beyerlein, Strength and ductility with {10 11}-{1012} double twinning in a magnesium alloy, Nat. Commun. 7 (2016) 1–7. https://doi.org/10.1038/ncomms11068.
- [54] D. Ando, J. Koike, Y. Sutou, The role of deformation twinning in the fracture behavior and mechanism of basal textured magnesium alloys, Mater. Sci. Eng. 600 (2014) 145–152. https://doi.org/10.1016/j.msea.2014.02.010.
- [55] X. Zhu, Y. Wang, L. Carneiro, H. Wang, Y. Jiang, Evaluation of elastic-viscoplastic self-consistent models for a rolled AZ31B magnesium alloy under monotonic loading along five different material orientations and free-end torsion, J. Magnes. Alloy (2021). In press, https://doi.org/10.1016/j.jma.2021.07.023.
- [56] S.R. Agnew, D.W. Brown, C.N. Tomé, Validating a polycrystal model for the elastoplastic response of magnesium alloy AZ31 using in situ neutron diffraction, Acta Mater. 54 (2006) 4841–4852, https://doi.org/10.1016/j. actamat 2006 06 020
- [57] L. Jiang, J.J. Jonas, R.K. Mishra, A.A. Luo, A.K. Sachdev, S. Godet, Twinning and texture development in two Mg alloys subjected to loading along three different strain paths, Acta Mater. 55 (2007) 3899–3910, https://doi.org/10.1016/j. actamat.2007.03.006.
- [58] T. Mukai, M. Yamanoi, H. Watanabe, K. Ishikawa, K. Higashi, Effect of grain refinement on tensile ductility in ZK60 magnesium alloy under dynamic loading, Mater. Trans. 42 (2001) 1177–1181.